Persymmetric Adaptive Detection and Range Estimation of a Small Target

Chengpeng Hao, *Member, IEEE,* Saeed Gazor, *Senior Member, IEEE,*
Goffredo Foglia, *Member, IEEE,* Bin Liu, *Member, IEEE,* Chaohuan Hou, *Fellow, IEEE,*

***Abstract*—In this paper, we address the problem of detecting relatively small targets in the presence of Gaussian disturbance with unknown covariance matrix. To this end, we jointly exploit the spillover of target energy to consecutive range samples and the particular persymmetric structure of the disturbance covariance matrix to improve the performances of detection and range localization. In this context, we derive two adaptive detectors relying on the generalized likelihood ratio test and on *ad hoc* design procedure. Remarkably, the new receivers ensure the constant false alarm rate property with respect to the disturbance covariance matrix. The performance assessments, conducted on both simulated data and real recorded datasets demonstrate the effectiveness of the proposed detectors compared with both the traditional unstructured counterparts and the state-of-the-art persymmetric detectors which ignore the spillover.**

***Index Terms*—Adaptive Detection, Range Estimation, Generalized Likelihood Ratio Test (GLRT), Persymmetry.**

I. Introduction

In recent years the design of space-time adaptive detection algorithms, that process data from antenna arrays, has received a vibrant attention from the radar community. Traditional space-time adaptive detectors (such as Reed, Mallet, and Brennan (RMB) detector [1], Kelly's Generalized Likelihood Ratio Test (GLRT) [2], the Adaptive Matched Filter (AMF) [3]–[5], the Rao test (RAO) [6], [7], and the Adaptive Beamformer Orthogonal Rejection Test (ABORT) [8]) are developed for homogeneous environments. Specifically, they require the estimate of the disturbance covariance matrix, performed through a sample covariance matrix, resorting to a secondary data set collected from range gates spatially close to the primary data and sharing the same spectral properties. In order to obtain performance within 3 dB from the optimum bound, it is well known that $K \geq 2N_aN_p$ Independent and Identically Distributed (IID) secondary data are required [9], [10], where N_a denotes the number of spatial channels and N_p the number of pulses contained in the coherent processing interval.

C. Hao and C. Hou are with State Key Laboratory of Information Technology for Autonomous Underwater vehicles, Chinese Academy of Sciences, 100190 Beijing, China. E-mail: haochengp@mail.ioa.ac.cn, hch@mail.ioa.ac.cn.

S. Gazor is with Department of Electrical and Computer Engineering, Queens University, K7L 3N6 Kingston, Ontario, Canada. E-mail: gazorg@queensu.ca.

G. Foglia is with ELETTRONICA S.p.A., Via Tiburtina Valeria, 00131 Rome, Italy. E-mail: goffredo.foglia@gmail.com.

B. Liu is with School of Computer Science and Technology, Nanjing University of Posts and Telecommunications, 210023 Nanjing, China. E-mail: bins@ieee.org.

In practical scenarios, the available number of the secondary data is not always large enough. This is commonly caused by many factors such as the presence of power variations over range, clutter edges, dense target environments, and other outliers [11]–[14]. One way to circumvent the lack of a sufficient amount of homogeneous secondary data is to exploit the persymmetric structure of the disturbance covariance matrix, which means that the covariance matrix is persymmetric about its cross diagonal. There are several radar applications in which the covariance matrix of the disturbance has this particular structure, e.g., in a system utilizing symmetrically spaced pulse trains or a symmetrically spaced linear array [15]. The utilization of persymmetric property can be traced back to [16] and is proven to be an effective way to mitigate the demanding requirement of homogeneous secondary data, because this structure involves less unknown parameters to characterize the unknown covariance matrix and hence allows to obtain an enhanced estimate of unknown parameters. Following [16], some adaptive detection schemes explicitly taking into account the persymmetric property have been proposed in [17]–[25]. More precisely, in [17], the persymmetric property is exploited to devise an adaptive detector for multiband signals. The extension of this idea to the case of partially homogeneous scenarios has been dealt with in [18]–[20], where the disturbance covariance matrices of the primary and secondary data have the same structure, but possibly different power levels. More recently, [21]–[23] address persymmetric adaptive detection in the presence of compound-Gaussian disturbance, while [24] considers the case that the disturbance is modeled as a multichannel Autoregressive (AR) process. Finally, two persymmetric adaptive detectors with enhanced rejection capabilities have been introduced in [25], whereas in [26] a systematic and unifying framework for persymmetric adaptive detection against homogenous scenarios has been proposed.

All the above mentioned detectors in [1]–[25] are based on the assumption that the target is exactly located at the corresponding sample time and, hence, they do not consider any spillover of target energy into the adjacent matched filter returns. In fact, such assumption is not always reasonable, because there is no guarantee that the samples at the matched filter output is exactly taken at the peak of the target return. The spillover is a physical phenomenon in a radar system and arises as the centroid of the received target pulse is somewhere between two consecutive range cells [27], [28]. Figure Ia illustrates the frequently encountered scenario in practice where a target straddles between the range cells n and

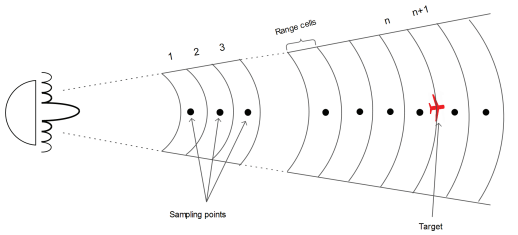

(a)

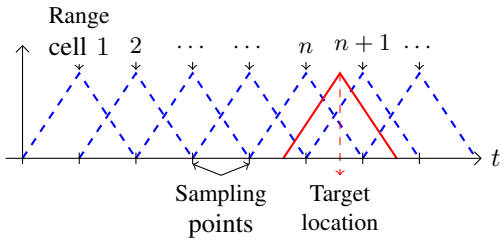

(b)

Fig. 1. a) The illustration of a target straddling between two consecutive range cells n and $n+1$; b) the cross-correlation function for a rectangular pulse versus the range locations and stampeded cells.

$n+1$ and the target location is not exactly an integer multiple of the range cell size of the radar. Accordingly, Figure Ib shows the crosscorrelation function for a rectangular pulse waveform for targets located exactly at the center of different range cells by blue dashed lines and by red color solid lines for a target straddling at an arbitrary location between the centers of two successive range cells n and $n+1$. The problem is similar in the Doppler dimension; that is, a target in general appears between two consecutive Doppler filters.

The spillover causes a significant loss in signal energy in the above traditional radar signal processing methods. Several methods have been proposed to mitigate or to take advantage of the energy split among adjacent samples. Actually, this spillover is shown to be a boon rather than a nuisance if it is properly processed. For example in [29] using two adjacent matched filter samples, it is shown that a monopulse radar may discern up to five targets instead of two by exploiting the spillover. This framework is further generalized in [30] to the case of space-time adaptive processing (STAP) [31], wherein a space-time spillover model for small targets is established and two detectors are introduced, namely the Modified GLRT (M-GLRT) and the Modified AMF (M-AMF). These methods exploit the spillover of target energy to provide accurate estimates of the target position within the cell under test.

In this paper, we extend the framework proposed in [30] to the design of receivers which simultaneously exploit the spillover of target energy and the persymmetric structure of the disturbance covariance matrix to enhance the performances of detection and range estimation. More precisely, we use the discrete-time model of the received signal in [30] and resort to both the GLRT and the so-called two-step GLRT-based design procedure [3], [32] assuming that a set of noise-only data is available. In other words, our incorporation of the persymmetric property in the M-GLRT and M-AMF leads to two new detectors, which greatly improves the robustness in training-limited scenarios by exploiting the persymmetric property which involves the estimation of less number of unknown parameters. Moreover, the novelty of the present work with respect to aforementioned persymmetric works is that the new persymmetric receivers take advantage of the spillover of target energy by exploiting the relationship between the amplitude of returns from the target not only in the CUT but also in two adjacent cells. This advantage comes from the considered space-time spillover model of targets, namely, the primary data include information not only at the CUT, but also at two adjacent cells because of the spillover. As a result, the new detectors guarantee superior detection performance with respect to the state-of-the-art persymmetric detectors which ignore the spillover. Moreover, they ensure superior range estimation, while the state-of-the-art persymmetric detectors do not have this ability. It is worth pointing out that we also derive a more general closed-form expression for the Maximum Likelihood (ML) estimation of the target radar cross section. Our results confirm these improvements on simulated data and real record data. The proposed methods have several applications/advantages. For example:

1) The enhanced accuracy in range can be extended to achieve enhanced accuracy in Doppler.
2) The enhanced range estimate not only can be fed to the conventional tracking stage (assuming the usual distinction between detection and tracking stages) [33], [34], but also can be used in the context of track-before-detect [35], [36] to further improve the radar tracking performance.
3) The proposed methods can be extended to detect and localize multiple point-like targets within adjacent samples [37], [38].

The remainder of this paper is organized as follows. Problem formulation is contained in Section II while Section III is devoted to detector designs. Section IV contains some illustrative examples. Finally, concluding remarks are given in Section V.

II. Problem Formulation

In this section, we briefly describe the multichannel discrete-time signal model (see [30], [39] for further details). Without loss of generality, let us consider a radar system equipped with a uniform linear array of N_a identical sensors with inter-element spacing d [40]. The radar illuminates the surveillance area by transmitting N_p coherent pulse, before deciding whether or not a target is present over consecutive samples. For simplicity, we suppose that the array is looking broadside, hence, that each sensor transmits the following coherent burst of pulses

$$\Re e\left\{A\sum_{n=1}^{N_p} p(t-(n-1)T)e^{j2\pi f_c t}\right\}, \quad t\in[0,N_pT) \quad (1)$$

where $\Re e\{z\}$ is the real part of the complex number z, A is the complex amplitude of the transmitted signal, $p(t)$ is a unit-energy arbitrary waveform (e.g., rectangular pulse waveform)

of duration T_p with a one-sided bandwidth of $W_p \approx 1/T_p$, T is the pulse repetition time, $f_c = c/\lambda$ is the carrier frequency with c the propagation velocity, and λ the wavelength. The range gates are formed by sampling the output of a filter matched to $p(t)$ every T_p seconds.

The signal backscattered from a target is first down converted to the baseband and then passed through a filter matched to $p(t)$. The output of this filter at ith sensor is given as

$$z_i(t) = \alpha e^{j2\pi(i-1)\nu_s} \sum_{n=1}^{N_p} \chi_p(t-(n-1)T-\tau, f) e^{j2\pi(n-1)\nu} + n_i(t) \quad i = 1, \ldots, N_a, \tag{2}$$

where $\chi_p(\cdot,\cdot)$ is the (complex) ambiguity function defined as [41]

$$\chi_p(\tau, f) = \int_{-\infty}^{+\infty} p(t) p^*(t-\tau) e^{j2\pi f t} dt \tag{3}$$

with $(\cdot)^*$ the complex conjugate operator, τ is the round-trip delay of the received signal, $\nu = fT$ is the Doppler frequency shift induced by the target motion with $f = \frac{2v}{c} f_c$, ν_s is the target normalized spatial frequency, i.e., $\nu_s = (d/\lambda)\cos\psi$, with ψ the polar angle of the target, $n_i(t)$ is the disturbance component (i.e., clutter and noise), and α is the complex magnitude of the signal, which is proportional to A, the transmitting antenna gain, the receiving antenna gain, the two-way path loss, and the radar cross section of the target.

The received signal at the ith sensor $z_i(t)$ is sampled at the following time instants

$$t_{l,n} = t_{\min} + (l-1)T_p + (n-1)T, \quad n = 1, \ldots, N_p, \quad l = 1, \ldots, L, \tag{4}$$

where $t_{\min}$ denotes the beginning of the sampling process, l is the range gate index, n is nth pulse from the same range cell, $L \in \mathbb{N}$ is the number of range gates representative of the surveillance area. Thus, by grouping the time samples, we can obtain the vector of the noisy returns representing the lth range "sub-cell" as follows

$$\boldsymbol{z}_l = \left[z_1(t_{l,1}) \ \cdots \ z_{N_a}(t_{l,1}) \ \cdots \ z_1(t_{l,N_p}) \ \cdots \ z_{N_a}(t_{l,N_p})\right]^T = \boldsymbol{s}_l + \boldsymbol{n}_l \in \mathbb{C}^{N\times 1}, \tag{5}$$

where $N = N_a N_p$, $(\cdot)^T$ denotes transpose, $\boldsymbol{n}_l$ is the disturbance component, and the signal component $\boldsymbol{s}_l$ is given by

$$\boldsymbol{s}_l = \begin{cases} \alpha\chi_p(-\epsilon_0, f)\boldsymbol{v}(\nu,\nu_s), & l = l_0 \\ \alpha\chi_p(T_p-\epsilon_0, f)\boldsymbol{v}(\nu,\nu_s), & l = l_0+1 \\ 0, & l \neq l_0, l_0+1, \end{cases} \tag{6}$$

with l_0 the sample under test, $\boldsymbol{v}$ the overall space-time steering vector (for the sake of brevity we omit the dependence of $\boldsymbol{v}$ on ν and ν_s.), and ϵ_0 a residual delay that leads to the spillover of target energy. The sampling process of the signal component is illustrated in Figure 2, where the radar waveform is assumed to be a unit-energy rectangular pulse waveform of duration T_p second.

Alternatively, we can define the residual delay ϵ evaluated with respect to the lth range sub-bin accounting for the target position surrounding the lth sub-bin center as follows

$$\epsilon = \begin{cases} \epsilon_0, & \text{if } l = l_0 \text{ and } 0 \le \epsilon_0 \le T_p/2, \\ \epsilon_0 - T_p, & \text{if } l = l_0+1 \text{ and } T_p/2 \le \epsilon_0 \le T_p. \end{cases} \tag{7}$$

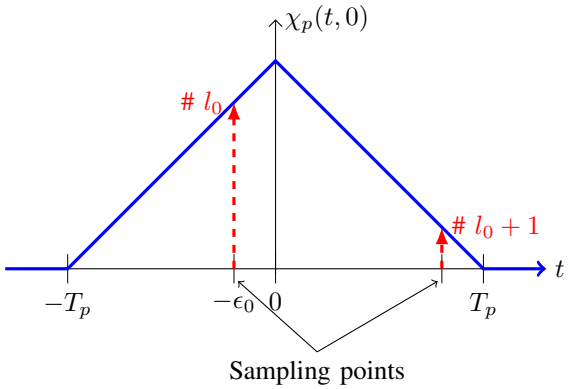

Fig. 2. Sampling process of the signal component assuming a unit-energy rectangular pulse waveform of duration T_p seconds.

We are interested in deciding whether or not a target is present across three adjacent range cells denoted by $\boldsymbol{z}_i$, $i = l-1, l, l+1$, in order to exploit the spillover of target energy. Meanwhile, we assume that a secondary data set $\boldsymbol{z}_k$, $k = 1, \ldots, K$, free of signal components, is available. It follows that the decision problem can be formulated as a binary hypothesis testing problem

$$\begin{cases} H_0 : \begin{cases} \boldsymbol{z}_i = \boldsymbol{n}_i, \ i = l-1, l, l+1, \\ \boldsymbol{z}_k = \boldsymbol{n}_k, \ k = 1, \ldots, K, \end{cases} \\ H_1 : \begin{cases} \boldsymbol{z}_{l-1} = \boldsymbol{n}_{l-1}, & 0 < \epsilon \le T_p/2, \\ \boldsymbol{z}_{l-1} = \alpha\chi_p(-T_p-\epsilon, f)\boldsymbol{v} + \boldsymbol{n}_{l-1}, & -T_p/2 \le \epsilon \le 0, \\ \boldsymbol{z}_l = \alpha\chi_p(-\epsilon, f)\boldsymbol{v} + \boldsymbol{n}_l, & \\ \boldsymbol{z}_{l+1} = \alpha\chi_p(T_p-\epsilon, f)\boldsymbol{v} + \boldsymbol{n}_{l+1}, & 0 < \epsilon \le T_p/2, \\ \boldsymbol{z}_{l+1} = \boldsymbol{n}_{l+1}, & -T_p/2 \le \epsilon \le 0, \\ \boldsymbol{z}_k = \boldsymbol{n}_k, & k = 1, \ldots, K, \end{cases} \end{cases} \tag{8}$$

where H_0 and H_1 denote the noise-only hypothesis and the signal-plus-noise hypothesis, respectively, $\boldsymbol{n}_i$, $i = l-1, l, l+1$, and $\boldsymbol{n}_k$, $k = 1, \ldots, K$, are independent, complex normal random vectors with zero mean and covariance matrix $\boldsymbol{M}$.

Finally, observe that for an active system utilizing symmetrically spaced linear array and/or pulsed train, both the disturbance covariance matrix $\boldsymbol{M}$ and the nominal steering vector $\boldsymbol{v}$ have the persymmetric property. More precisely, $\boldsymbol{M}$ belongs to the set $\mathcal{P}$ defined as

$$\boldsymbol{M} \in \mathcal{P} \quad \text{iff} \quad \boldsymbol{M} = \boldsymbol{J}_N \boldsymbol{M}^* \boldsymbol{J}_N, \tag{9}$$

and $\boldsymbol{v} = \boldsymbol{J}_N \boldsymbol{v}^*$, where $\boldsymbol{J}_N \in \mathbb{R}^{N\times N}$ is the permutation matrix, i.e.,

$$\boldsymbol{J}_N = \begin{bmatrix} 0 & 0 & \cdots & 0 & 1 \\ 0 & 0 & \cdots & 1 & 0 \\ \vdots & \iddots & \iddots & \iddots & \vdots \\ 1 & 0 & \cdots & 0 & 0 \end{bmatrix}. \tag{10}$$

Using above framework, we solve the problem in (8) by using the GLRT and an *ad hoc* procedure, leading to adaptive decision schemes which exploit the spillover of target energy and the structure of disturbance covariance matrix (as shown in the next sections).

III. Detector Designs

As a preliminary step towards the derivation of the detectors, let us denote by $\boldsymbol{Z} = [\boldsymbol{Z}_L \ \boldsymbol{Z}_K] \in \mathbb{C}^{N\times(K+3)}$ the overall data

matrix, with $\boldsymbol{Z}_L = [\boldsymbol{z}_{l-1}, \boldsymbol{z}_l, \boldsymbol{z}_{l+1}] \in \mathbb{C}^{N\times 3}$ the primary data matrix and $\boldsymbol{Z}_K = [\boldsymbol{z}_1, \ldots, \boldsymbol{z}_K] \in \mathbb{C}^{N\times K}$ the secondary data matrix, and

$$\boldsymbol{\chi}(\epsilon) = \begin{cases} [\chi_p(-T_p-\epsilon, f), \chi_p(-\epsilon, f), 0]^T, & -T_p/2 \le \epsilon \le 0, \\ [0, \chi_p(-\epsilon, f), \chi_p(T_p-\epsilon, f)]^T, & 0 < \epsilon \le T_p/2. \end{cases} \tag{11}$$

A. One-Step GLRT-Based Detector

The GLRT based on primary and secondary data is given by [42]

$$\frac{\max\limits_{\epsilon,\alpha,\mathbf{M}} f_1(\boldsymbol{Z}; \boldsymbol{M}, \alpha, \epsilon)}{\max\limits_{\mathbf{M}} f_0(\boldsymbol{Z}; \boldsymbol{M})} \underset{H_0}{\overset{H_1}{\gtrless}} \eta, \tag{12}$$

where η is the threshold value to be set according to the desired probability of false alarm (P_{fa}), and $f_j(\boldsymbol{Z}; \cdot)$ is the Probability Density Function (PDF) of $\boldsymbol{Z}$ under H_j, $j = 0, 1$, namely [43]

$$f_1(\boldsymbol{Z}; \boldsymbol{M}, \alpha, \epsilon) = \left[\frac{1}{\pi^N \det(\boldsymbol{M})}\right]^{K+3} \exp\left\{-\text{tr}\left[\boldsymbol{M}^{-1}\boldsymbol{T}_1\right]\right\},$$
$$f_0(\boldsymbol{Z}; \boldsymbol{M}) = \left[\frac{1}{\pi^N \det(\boldsymbol{M})}\right]^{K+3} \exp\left\{-\text{tr}\left[\boldsymbol{M}^{-1}\boldsymbol{T}_0\right]\right\}. \tag{13}$$

In (13), $(\cdot)^H$ denotes conjugate transpose, $\det(\cdot)$ and $\text{tr}(\cdot)$ denote the determinant and the trace of a square matrix, respectively, and

$$\begin{aligned} \boldsymbol{T}_1 &= \left[\boldsymbol{Z}_L - \alpha\boldsymbol{v}\boldsymbol{\chi}^T(\epsilon)\right]\left[\boldsymbol{Z}_L - \alpha\boldsymbol{v}\boldsymbol{\chi}^T(\epsilon)\right]^H + \boldsymbol{S}, \\ \boldsymbol{T}_0 &= \boldsymbol{Z}_L\boldsymbol{Z}_L^H + \boldsymbol{S} \end{aligned} \tag{14}$$

with $\boldsymbol{S} = \boldsymbol{Z}_K\boldsymbol{Z}_K^H$ the K times sample covariance matrix of the secondary data.

Exploiting the persymmetric properties of $\boldsymbol{M}$ and $\boldsymbol{v}$, we have the following trace equality (see [16] for more details)

$$\text{tr}\left[\boldsymbol{M}^{-1}\boldsymbol{T}_j\right] = \text{tr}\left[\boldsymbol{M}^{-1}\frac{\boldsymbol{T}_j + \boldsymbol{J}_N\boldsymbol{T}_j^*\boldsymbol{J}_N}{2}\right], \ j = 0, 1. \tag{15}$$

It follows that the PDF of $\boldsymbol{Z}$ under both hypothesis can be rewritten as follows

$$\begin{aligned} f_1(\boldsymbol{Z}; \boldsymbol{M}, \boldsymbol{\alpha}_p, \epsilon) &= \left[\frac{1}{\pi^N \det(\boldsymbol{M})}\right]^{K+3} \\ &\times \exp\left\{-\text{tr}\left[\boldsymbol{M}^{-1}\left(\boldsymbol{F}\boldsymbol{F}^H + \boldsymbol{S}_p\right)\right]\right\}, \\ f_0(\boldsymbol{Z}; \boldsymbol{M}) &= \left[\frac{1}{\pi^N \det(\boldsymbol{M})}\right]^{K+3} \\ &\times \exp\left\{-\text{tr}\left[\boldsymbol{M}^{-1}\left(\boldsymbol{X}_p\boldsymbol{X}_p^H + \boldsymbol{S}_p\right)\right]\right\}, \end{aligned} \tag{16}$$

where

$$\boldsymbol{F} = \boldsymbol{X}_p - \boldsymbol{v}\boldsymbol{\alpha}_p\boldsymbol{D}^T(\epsilon), \tag{17}$$

$$\boldsymbol{D}(\epsilon) = \begin{cases} \begin{bmatrix} \chi_p(t_1,f), & \chi_p(t_1,f), & \chi_p(t_2,f), & \chi_p(t_2,f), & 0, & 0 \\ \chi_p^*(t_1,f), & -\chi_p^*(t_1,f), & \chi_p^*(t_2,f), & -\chi_p^*(t_2,f), & 0, & 0 \end{bmatrix}^T, \\ \qquad\qquad \text{if } -T_p/2 \le \epsilon \le 0 \\ \begin{bmatrix} 0, & 0, & \chi_p(t_2,f), & \chi_p(t_2,f), & \chi_p(t_3,f), & \chi_p(t_3,f) \\ 0, & 0, & \chi_p^*(t_2,f), & -\chi_p^*(t_2,f), & \chi_p^*(t_3,f), & -\chi_p^*(t_3,f) \end{bmatrix}^T, \\ \qquad\qquad \text{if } 0 < \epsilon \le T_p/2, \end{cases}$$

with $t_1 = -T_p - \epsilon$, $t_2 = -\epsilon$, $t_3 = T_p - \epsilon$, and

$$\begin{aligned} \boldsymbol{S}_p &= (\boldsymbol{S} + \boldsymbol{J}_N\boldsymbol{S}^*\boldsymbol{J}_N)/2, \ \boldsymbol{\alpha}_p = [\alpha, \alpha^*], \\ \boldsymbol{X}_p &= [\boldsymbol{z}_{e_{l-1}}, \boldsymbol{z}_{o_{l-1}}, \boldsymbol{z}_{e_l}, \boldsymbol{z}_{o_l}, \boldsymbol{z}_{e_{l+1}}, \boldsymbol{z}_{o_{l+1}}] \end{aligned} \tag{18}$$

with $\boldsymbol{z}_{e_k} = (\boldsymbol{z}_k + \boldsymbol{J}_N\boldsymbol{z}_k^*)/2$, and $\boldsymbol{z}_{o_k} = (\boldsymbol{z}_k - \boldsymbol{J}_N\boldsymbol{z}_k^*)/2$, $k = l-1, l, l+1$. Note that we must have $K \ge N/2$ in order to maintain a nonsingular sample covariance matrix whereas we must have $K \ge N$ if the structure of the covariance matrix is not exploited.

Let us first solve the optimization problem under H_1. To this end, observe that the maximum likelihood estimate of $\boldsymbol{M}$ is given by the sample covariance matrix [2], namely

$$\widehat{\boldsymbol{M}} = \frac{1}{K+3}\left(\boldsymbol{F}\boldsymbol{F}^H + \boldsymbol{S}_p\right). \tag{19}$$

From (14) and (19), we obtain $\boldsymbol{T}_1 = (K+3)\widehat{\boldsymbol{M}}$, which, by substituting into (15), yields

$$\text{tr}\left[\boldsymbol{M}^{-1}\widehat{\boldsymbol{M}}\right] = \text{tr}\left[\boldsymbol{M}^{-1}\frac{\widehat{\boldsymbol{M}} + \boldsymbol{J}_N\widehat{\boldsymbol{M}}^*\boldsymbol{J}_N}{2}\right]. \tag{20}$$

Note that (20) states that the traces of these matrices are equal, while the matrices $\boldsymbol{M}^{-1}\widehat{\boldsymbol{M}}$ and $\boldsymbol{M}^{-1}\frac{\widehat{\boldsymbol{M}}+\boldsymbol{J}_N\widehat{\boldsymbol{M}}^*\boldsymbol{J}_N}{2}$ may be equal or not. In other words, the matrix $\widehat{\boldsymbol{M}}$ is not necessarily a persymmetric, irrespective of $\boldsymbol{\alpha}_p$.

Substitution of $\widehat{\boldsymbol{M}}$ into (16) yields that $f_1(\boldsymbol{Z}; \widehat{\boldsymbol{M}}, \boldsymbol{\alpha}_p, \epsilon)$ is proportional to

$$\det\left[\boldsymbol{F}\boldsymbol{F}^H + \boldsymbol{S}_p\right]^{-(K+3)}. \tag{21}$$

Maximizing (21) over $\boldsymbol{\alpha}_p$ is tantamount to the following minimization

$$\min_{\boldsymbol{\alpha}_p} \ \det\left[\boldsymbol{F}\boldsymbol{F}^H + \boldsymbol{S}_p\right], \tag{22}$$

where the argument can be recast as follows

$$\begin{aligned} &\det\left[\boldsymbol{F}\boldsymbol{F}^H + \boldsymbol{S}_p\right] \\ &= \det[\boldsymbol{S}_p]\det\left[\boldsymbol{I}_6 + \boldsymbol{F}^H\boldsymbol{S}_p^{-1}\boldsymbol{F}\right] \\ &= \det[\boldsymbol{S}_p]\det\left[\boldsymbol{I}_6 + \boldsymbol{F}^H\boldsymbol{S}_p^{-1/2}\left(\boldsymbol{P}_{\boldsymbol{v}_s}^{\perp} + \boldsymbol{P}_{\boldsymbol{v}_s}\right)\boldsymbol{S}_p^{-1/2}\boldsymbol{F}\right] \\ &= \det[\boldsymbol{S}_p]\det\left[\boldsymbol{Q} + \boldsymbol{F}^H\boldsymbol{S}_p^{-1/2}\boldsymbol{P}_{\boldsymbol{v}_s}\boldsymbol{S}_p^{-1/2}\boldsymbol{F}\right] \\ &= \det[\boldsymbol{S}_p]\det[\boldsymbol{Q}]\left[1 + \frac{\boldsymbol{v}^H\boldsymbol{S}_p^{-1}\boldsymbol{F}\boldsymbol{Q}^{-1}\boldsymbol{F}^H\boldsymbol{S}_p^{-1}\boldsymbol{v}}{\boldsymbol{v}^H\boldsymbol{S}^{-1}\boldsymbol{v}}\right] \end{aligned} \tag{23}$$

with $\boldsymbol{I}_N$ the N-dimensional identity matrix, $\boldsymbol{P}_{\boldsymbol{v}_s} = \boldsymbol{v}_s\left(\boldsymbol{v}_s^H\boldsymbol{v}_s\right)^{-1}\boldsymbol{v}_s^H$ the projection matrix onto the subspace spanned by $\boldsymbol{v}_s = \boldsymbol{S}_p^{-1/2}\boldsymbol{v}$, $\boldsymbol{P}_{\boldsymbol{v}_s}^{\perp} = \boldsymbol{I}_N - \boldsymbol{P}_{\boldsymbol{v}_s}$ the projection matrix onto the orthogonal complement of the space spanned by $\boldsymbol{v}_s$, and

$$\boldsymbol{Q} = \boldsymbol{I}_6 + \boldsymbol{X}_p^H\boldsymbol{S}_p^{-1/2}\boldsymbol{P}_{\boldsymbol{v}_s}^{\perp}\boldsymbol{S}_p^{-1/2}\boldsymbol{X}_p. \tag{24}$$

Thus, the optimization problem (22) is equivalent to

$$\min_{\boldsymbol{\alpha}_p} \ \boldsymbol{v}^H\boldsymbol{S}_p^{-1}\boldsymbol{F}\boldsymbol{Q}^{-1}\boldsymbol{F}^H\boldsymbol{S}_p^{-1}\boldsymbol{v}. \tag{25}$$

Based on the expression (25), a closed-form estimate of $\boldsymbol{\alpha}_p$ is given by (see Appendix A for the proof)

$$\widehat{\boldsymbol{\alpha}}_p = \frac{\boldsymbol{v}^H \boldsymbol{S}_p^{-1} \boldsymbol{X}_p \boldsymbol{Q}^{-1} \boldsymbol{D}^*(\epsilon) \left[\boldsymbol{D}^T(\epsilon) \boldsymbol{Q}^{-1} \boldsymbol{D}^*(\epsilon)\right]^{-1}}{\boldsymbol{v}^H \boldsymbol{S}_p^{-1} \boldsymbol{v}}. \quad (26)$$

It follows that the compressed likelihood function under H_1 can be written as

$$f_1(\boldsymbol{Z}; \widehat{\boldsymbol{M}}, \widehat{\boldsymbol{\alpha}}_p, \epsilon) \propto \det\left[\boldsymbol{F}_a \boldsymbol{F}_a^H + \boldsymbol{S}_p\right]^{-(K+3)}, \quad (27)$$

where $\propto$ stands for proportionality, and $\boldsymbol{F}_a$ is obtained by substituting $\boldsymbol{\alpha}_p$ with $\widehat{\boldsymbol{\alpha}}_p$ in (17).

On the other hand, the compressed likelihood function under H_0 is given by

$$f_0(\boldsymbol{Z}; \widehat{\boldsymbol{M}}) \propto \det\left[\boldsymbol{X}_p \boldsymbol{X}_p^H + \boldsymbol{S}_p\right]^{-(K+3)}. \quad (28)$$

Finally, the GLRT (12) can be recast as

$$\max_{\epsilon \in [-T_p/2, T_p/2]} \frac{\det\left[\boldsymbol{X}_p \boldsymbol{X}_p^H + \boldsymbol{S}_p\right]}{\det\left[\boldsymbol{F}_a \boldsymbol{F}_a^H + \boldsymbol{S}_p\right]} \underset{H_0}{\overset{H_1}{\gtrless}} \eta, \quad (29)$$

where η is the suitable modification of the threshold in (12). In Appendix B, it is shown that this test is equivalent to

$$\max_{\epsilon \in [-T_p/2, T_p/2]} \frac{\boldsymbol{v}^H \boldsymbol{S}_p^{-1} \boldsymbol{X}_p \boldsymbol{W}(\epsilon) \boldsymbol{X}_p^H \boldsymbol{S}_p^{-1} \boldsymbol{v}}{\boldsymbol{v}^H \boldsymbol{S}_p^{-1} \boldsymbol{v} + \boldsymbol{v}^H \boldsymbol{S}_p^{-1} \boldsymbol{X}_p \boldsymbol{Q}^{-1} \boldsymbol{X}_p^H \boldsymbol{S}_p^{-1} \boldsymbol{v}} \underset{H_0}{\overset{H_1}{\gtrless}} \eta. \quad (30)$$

where

$$\boldsymbol{W}(\epsilon) = \boldsymbol{Q}^{-1} \boldsymbol{D}^*(\epsilon) \left[\boldsymbol{D}^T(\epsilon) \boldsymbol{Q}^{-1} \boldsymbol{D}^*(\epsilon)\right]^{-1} \boldsymbol{D}^T(\epsilon) \boldsymbol{Q}^{-1}. \quad (31)$$

Since a closed-form estimate of ϵ is not available, we resort to a grid search to maximize with respect to ϵ. More precisely, ϵ takes on values in $\Omega \equiv \left\{\frac{n - N_\epsilon}{2N_\epsilon} T_p\right\}_{\eta=0}^{2N_\epsilon}$ with $N_\epsilon \in \mathbb{N}$. This detector with an grid-search-based implementation will be referred to in the sequel as the Persymmetric Modified Kelly's GLRT (P-M-GLRT).

B. Two-Step GLRT-Based Detector

This section is devoted to the derivation of an *ad hoc* detector based upon the two-step GLRT-based design procedure [3]. The rationale of the design procedure is the following: first assume that the covariance matrix $\boldsymbol{M} \in \mathcal{P}$ is known and derive the GLRT based on primary data. Then, an adaptive detector is obtained by substituting $\boldsymbol{M}$ by the structured covariance matrix estimate $\boldsymbol{S}_p$.

Under the assumption that $\boldsymbol{M}$ is known, the GLRT is given by

$$\frac{\max_{\epsilon, \alpha} f_1(\boldsymbol{Z}_L; \boldsymbol{M}, \alpha, \epsilon)}{f_0(\boldsymbol{Z}_L; \boldsymbol{M})} \underset{H_0}{\overset{H_1}{\gtrless}} \eta, \quad (32)$$

where $f_j(\boldsymbol{Z}_L; \cdot)$ is the PDF of $\boldsymbol{Z}_L$ under H_j, $j = 0, 1$, namely

$$\begin{aligned} f_1(\boldsymbol{Z}_L; \boldsymbol{M}, \alpha, \epsilon) &= \left[\frac{1}{\pi^N \det(\boldsymbol{M})}\right]^3 \\ &\quad \times \exp\left\{-\mathrm{tr}\left[\boldsymbol{M}^{-1}(\boldsymbol{T}_1 - \boldsymbol{S})\right]\right\}, \\ f_0(\boldsymbol{Z}_L; \boldsymbol{M}) &= \left[\frac{1}{\pi^N \det(\boldsymbol{M})}\right]^3 \\ &\quad \times \exp\left\{-\mathrm{tr}\left[\boldsymbol{M}^{-1}(\boldsymbol{T}_0 - \boldsymbol{S})\right]\right\}. \end{aligned} \quad (33)$$

Similarly, the above PDF can be expressed in persymmetric form, i.e.,

$$\begin{aligned} f_1(\boldsymbol{Z}_L; \boldsymbol{M}, \boldsymbol{\alpha}_p, \epsilon) &= \left[\frac{1}{\pi^N \det(\boldsymbol{M})}\right]^3 \\ &\quad \times \exp\left\{-\mathrm{tr}\left[\boldsymbol{M}^{-1}\left(\boldsymbol{F}\boldsymbol{F}^H\right)\right]\right\}, \\ f_0(\boldsymbol{Z}_L; \boldsymbol{M}) &= \left[\frac{1}{\pi^N \det(\boldsymbol{M})}\right]^3 \\ &\quad \times \exp\left\{-\mathrm{tr}\left[\boldsymbol{M}^{-1}\boldsymbol{X}_p\boldsymbol{X}_p^H\right]\right\}, \end{aligned} \quad (34)$$

where $\boldsymbol{X}_p$ and $\boldsymbol{\alpha}_p$ are given by (18). Substituting (34) in (32), after some algebraic manipulations, the natural logarithm of left-hand side of (32) can be recast as

$$\max_{\epsilon}\left\{\mathrm{tr}\left[\boldsymbol{M}^{-1}\boldsymbol{X}_p\boldsymbol{X}_p^H\right] - \min_{\boldsymbol{\alpha}_p} \mathrm{tr}\left[\boldsymbol{M}^{-1}\left(\boldsymbol{F}\boldsymbol{F}^H\right)\right]\right\}. \quad (35)$$

In order to optimize (35) with respect to $\boldsymbol{\alpha}_p$, it is shown in Appendix C that

$$\begin{aligned} &\mathrm{tr}\left[\boldsymbol{M}^{-1}\left(\boldsymbol{F}\boldsymbol{F}^H\right)\right] \\ &\quad = \mathrm{tr}\left[\boldsymbol{X}_p^H\boldsymbol{M}^{-1}\boldsymbol{X}_p\right] - (\boldsymbol{v}^H\boldsymbol{M}^{-1}\boldsymbol{v})\mathrm{tr}\left[\boldsymbol{D}^*(\epsilon)\boldsymbol{b}^H\boldsymbol{b}\boldsymbol{D}^T(\epsilon)\right] \\ &\quad +(\boldsymbol{v}^H\boldsymbol{M}^{-1}\boldsymbol{v})\mathrm{tr}\left[\left([\boldsymbol{\alpha}_p - \boldsymbol{b}]\boldsymbol{D}^T(\epsilon)\right)^H\left([\boldsymbol{\alpha}_p - \boldsymbol{b}]\boldsymbol{D}^T(\epsilon)\right)\right], \end{aligned} \quad (36)$$

where

$$\boldsymbol{b} = \frac{\boldsymbol{v}^H\boldsymbol{M}^{-1}\boldsymbol{X}_p\boldsymbol{D}^*(\epsilon)\left(\boldsymbol{D}^T(\epsilon)\boldsymbol{D}^*(\epsilon)\right)^{-1}}{\boldsymbol{v}^H\boldsymbol{M}^{-1}\boldsymbol{v}}. \quad (37)$$

It is clear that the minimum of (36) is attained when the positive factor containing $\boldsymbol{\alpha}_p$ is made to vanish, i.e., $\widehat{\boldsymbol{\alpha}}_p = \boldsymbol{b}$. Thus, the GLRT for known $\boldsymbol{M}$ can be recast as (see Appendix C for the detailed derivation)

$$\max_{\epsilon \in [-T_p/2, T_p/2]} \frac{\boldsymbol{v}^H\boldsymbol{M}^{-1}\boldsymbol{X}_p\boldsymbol{V}(\epsilon)\boldsymbol{X}_p^H\boldsymbol{M}^{-1}\boldsymbol{v}}{\boldsymbol{v}^H\boldsymbol{M}^{-1}\boldsymbol{v}} \underset{H_0}{\overset{H_1}{\gtrless}} \eta, \quad (38)$$

where η is the suitable modification of the threshold in (32), and

$$\boldsymbol{V}(\epsilon) = \boldsymbol{D}^*(\epsilon)\left(\boldsymbol{D}^T(\epsilon)\boldsymbol{D}^*(\epsilon)\right)^{-1}\boldsymbol{D}^T(\epsilon). \quad (39)$$

Plugging $\boldsymbol{S}_p$ in place of $\boldsymbol{M}$ into (38), a fully adaptive detector can be given by

$$\max_{\epsilon \in [-T_p/2, T_p/2]} \frac{\boldsymbol{v}^H\boldsymbol{S}_p^{-1}\boldsymbol{X}_p\boldsymbol{V}(\epsilon)\boldsymbol{X}_p^H\boldsymbol{S}_p^{-1}\boldsymbol{v}}{\boldsymbol{v}^H\boldsymbol{S}_p^{-1}\boldsymbol{v}} \underset{H_0}{\overset{H_1}{\gtrless}} \eta, \quad (40)$$

This detector with an grid-search-based implementation will be referred to in the sequel as the Persymmetric Modified AMF (P-M-AMF).

Remark 1: The P-M-GLRT and the P-M-AMF ensure the constant false alarm rate (CFAR) property with respect to $\boldsymbol{M}$. Moreover, they are computationally more efficient than the M-GLRT and the M-AMF. This is because the calculations of their statistics can be transferred from the complex domain to the real domain. Proofs of such statements, not reported here for the sake of brevity, follow the lead of [2], [17] and references therein.

Remark 2: Since $\boldsymbol{W}(\epsilon)$ and $\boldsymbol{V}(\epsilon)$ are functions of ϵ, they need to be calculated for each ϵ value which involve an additional computation burden. Anyway, the P-M-GLRT involves $O(KN^2)$ floating-point operations (flops) plus $O(6N^2 + 6^2N+6^3+(2N_\epsilon+1)6^2)$ fixed-point operations, whereas the P-M-AMF requires $O(KN^2)$ flops plus $O(6N^2+(2N_\epsilon+1)6^2)$ fixed-point operations. Note that the $O(n)$ is usual Landau notation and means that the implementation requires a number of flops proportional to n [44]. As to the persymmetric GLRT (P-GLRT) [17], the persymmetric adaptive matched filter (P-AMF) [23], they require $O(KN^2)$ flops plus $O(2N^2+4N+8)$ fixed-point operations, and $O(KN^2)$ flops plus $O(2N^2)$ fixed-point operations, respectively.

Remark 3: From the similarity of the expressions in (30) and (40), we expect that the performance gap between these tests is reduced as the size of the secondary data increases, since $\boldsymbol{Q}$ and $\boldsymbol{v}^H\boldsymbol{S}_p^{-1}\boldsymbol{X}_p\boldsymbol{Q}^{-1}\boldsymbol{X}_p^H\boldsymbol{S}_p^{-1}\boldsymbol{v}$ tend to $\boldsymbol{I}_6$ and 0, respectively.

Remark 4: Let $\hat{\epsilon}$ denote the value for which (30), (38) or (40) are maximized. To perform the maximization the values of these criterions are first calculated for N_ϵ values of ϵ equally spaced in the interval $[-\frac{T_p}{2}, -\frac{T_p}{2}]$, then the maximum value is compared with a threshold. In this case the range is estimated by $(t_{\min}+lT_p+\hat{\epsilon})\frac{c}{2}$ in meters where c is the wave propagation velocity.

IV. Performance Assessment

In this section, we present some numerical examples to show the performances of the proposed receivers in terms of probability of detection and root root mean square (RMS) error in range. To this end, we first compare our detectors to their unstructured counterparts, namely the M-GLRT and M-AMF introduced in [30]. Second, the new receivers are compared to the state-of-the-art persymmetric detectors which ignore the spillover of target energy and are devised for Gaussian disturbance, including the P-GLRT, the P-AMF, and the persymmetric adaptive coherence estimator (P-ACE) [20]. The analysis is conducted both on simulated and real recorded data.

A. Simulated data

For simulation purposes, we exploit standard Monte Carlo counting techniques and evaluate the thresholds necessary to ensure a preassigned value of $P_{\rm fa}$ resorting to $100/P_{\rm fa}$ independent trials. More precisely, the $P_{\rm d}$ values and the RMS range errors are estimated over 10^4 and 10^3 independent trials, respectively. All the illustrative examples assume $P_{\rm fa}=10^{-4}$, $T_p = 0.2\mu s$, $c = 3\times 10^8 m/s$, $f = 0$, and $N_\epsilon = 5$. The steering vector $\boldsymbol{v}$ is given by

$$\boldsymbol{v} = [1,\ldots,1]^T/\sqrt{N}, \tag{41}$$

and the signal-to-noise ratio (SNR) is defined as

$$\text{SNR} = |\alpha|^2\boldsymbol{v}^H\boldsymbol{M}^{-1}\boldsymbol{v}. \tag{42}$$

Our simulator requires α, N, K, T_p, f, and $\boldsymbol{v}$ as input and generate $\boldsymbol{Z}_L$ and $\boldsymbol{Z}_K$ as follows. We generate the actual position of the target $\epsilon_{\rm true}$ randomly and uniformly distributed over (independent from trial to trial and independent of all other generated parameters) over

$$(t_{\min}+(l-1)T_p - T_p/2,\ t_{\min}+(l-1)T_p+T_p/2)\,. \tag{43}$$

To facilitate the simulation, we set $t_{\min}=0$ and $l=1$, namely, the actual position of the target is uniformly distributed in $(-T_p/2, T_p/2)$. We then calculate $\boldsymbol{\chi}(\epsilon_{true})$ using (11). The noise samples $\boldsymbol{n}_i$, $i=l-1,l,l+1$ and $\boldsymbol{n}_k$, $k=1,\ldots,K$ are generated as independent, zero-mean complex normal random vectors with one-lag correlation coefficient ρ, namely the (i,j)-th element of the covariance matrix $\boldsymbol{M}$ is given by $\rho^{|i-j|}$, with $\rho=0.9$. The primary data matrix $\boldsymbol{Z}_L$ is obtained from

$$\boldsymbol{Z}_L = \alpha\boldsymbol{v}\boldsymbol{\chi}^T(\epsilon_{\rm true}) + \boldsymbol{N}_L, \tag{44}$$

where $\boldsymbol{N}_L = [\boldsymbol{n}_{l-1}, \boldsymbol{n}_l, \boldsymbol{n}_{l+1}]$, and the secondary data matrix from

$$\boldsymbol{Z}_K = [\boldsymbol{n}_1,\ldots,\boldsymbol{n}_K]\,. \tag{45}$$

Once $\boldsymbol{Z}_L$ and $\boldsymbol{Z}_K$ are obtained, we calculate the decision statistic of the P-M-GLRT/P-M-AMF for all $\epsilon\in\Omega$, and use the procedure in *Remark 4* to find the optimal estimate of $\epsilon_{\rm true}$, $\hat{\epsilon}_k$ say, where k is the index of trials. Finally, the average RMS range error (in meters) of the P-M-GLRT/P-M-AMF versus SNR is calculated using by

$$\delta_{\rm rms} = \sqrt{\frac{\sum_{k=1}^{n_e}(\hat{\epsilon}_k-\epsilon_{\rm true})*10^{-6}*c/2)^2}{n_e}}, \tag{46}$$

where n_e is the number of trials.

1) Comparison with localization detectors: In Figures 3 and 4, we compare the P-M-GLRT and P-M-AMF to the M-GLRT and M-AMF assuming $N=17$, $K=N+1$ in order to reflect the training-limited scenarios. In particular, in Figure 3 we plot $P_{\rm d}$ versus SNR, while in Figure 4 the comparison is in terms of RMS error in range. Moreover, the $P_{\rm d}$ curves of the optimum but nonadaptive versions of the proposed detectors, i.e., the P-M-GLRT and P-M-AMF with the known covariance matrix (refereed as the P-M-GLRT-OPT and P-M-AMF-OPT, respectively), are included in Figure 3 as benchmark.

Inspection of Figures 3 and 4 highlights that with such a limited amount of secondary data, the M-GLRT and M-AMF exhibit unsatisfactory performances, and the proposed detectors are a viable mean to compensate for the loss experienced

by the detectors which consider the spilover, although they still have some distance from the optimum. More precisely, Figure 3 shows that P-M-GLRT has the best performance of $P_{\rm d}$, while the P-M-AMF only experiences a loss of about 1.1 dB at $P_{\rm d} = 0.9$. However, such a loss increases to about 10.6 dB and 20.6 dB for the M-GLRT and the M-AMF, respectively. On the other hand, Figure 4 shows that the range RMS errors of the P-M-GLRT and P-M-AMF are about 1.7 m when SNR $= 25$ dB, and such RMS error increases to about 3.2 m and 3.7 m for the M-GLRT and M-AMF, respectively [1]. As to high SNR values, the range RMS errors of the four receivers are identical, due to the fact that in this case the RMS errors are determined by the grid resolution $\Delta_\epsilon = T_p/(2N_\epsilon)$. As a matter of fact, a uniformly distributed random variable in $(-\frac{\Delta}{2},\frac{\Delta}{2})$ with $\Delta = \Delta_\epsilon c/2$, has a standard deviation equal to $\frac{\Delta}{\sqrt{12}}$, which means a lower-bound on the RMS error of 0.866 m for $N_\epsilon = 5$ [30].

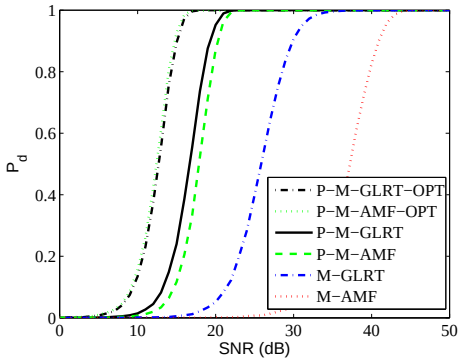

Fig. 3. $P_{\rm d}$ versus SNR for the P-M-GLRT, P-M-AMF, M-GLRT, and M-AMF with simulated data; $N = 17$, $K = N+1$, $N_\epsilon = 5$, and $P_{\rm fa} = 10^{-4}$.

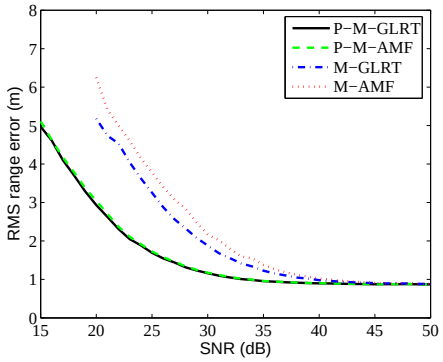

Fig. 4. RMS range error versus SNR for the P-M-GLRT, P-M-AMF, M-GLRT, and M-AMF with simulated data; $N = 17$, $K = N + 1$, $N_\epsilon = 5$, and $P_{\rm fa} = 10^{-4}$.

In Figures 5 and 6, $P_{\rm d}$ and range RMS error curves are shown assuming the same scenario as in Figures 3 and 4 but $K = 2N$. As it can be seen from these two figures, the receivers can take advantage of the higher number of secondary data. Specifically, the performances of the M-GLRT and M-AMF significantly improve with respect to the case $K = N + 1$, but they are still outperformed by the proposed detectors. This is not surprising, since the higher number of secondary data allows to better estimate the unknown parameters. It is also seen from Figure 5 that the P-M-GLRT performs very close to the P-M-AMF and experiences a loss of about 0.3 dB at $P_d = 0.9$. This result is aligned with what we expect in remark 2.

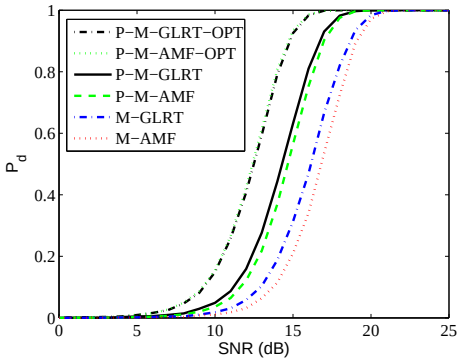

Fig. 5. $P_{\rm d}$ versus SNR for the P-M-GLRT, P-M-AMF, M-GLRT, and M-AMF with simulated data; $N = 17$, $K = 2N$, $N_\epsilon = 5$, and $P_{\rm fa} = 10^{-4}$.

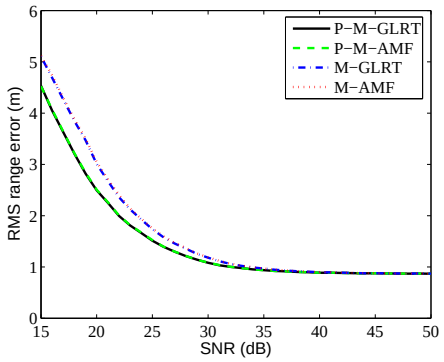

Fig. 6. RMS range error versus SNR for the P-M-GLRT, P-M-AMF, M-GLRT, and M-AMF with simulated data; $N = 17$, $K = 2N$, $N_\epsilon = 5$, and $P_{\rm fa} = 10^{-4}$.

2) Comparison with persymmetric detectors: To demonstrate the efficiency of the proposed detectors further, in Figures 7 and 8, we compare new receivers with the state-of-the-art persymmetric detectors. Therein we plot $P_{\rm d}$ versus SNR for the P-M-GLRT, P-M-AMF, P-GLRT, P-AMF, and P-ACE assuming $N = 8$, and two values of K. The figures show that the P-M-GLRT and P-M-AMF ensure better detection performance than the other persymmetric detectors. Obviously, the obtained $P_{\rm d}$ gains result from the use of the spillover of target energy. We do not evaluate the range RMS errors for these detectors, because the P-GLRT, P-AMF, and P-ACE do not have the ability of sub-bin range localization.

Our performed evaluations highlights that the proposed receivers allow simultaneous use of a-priori structure of the disturbance covariance matrix and the spillover of target

[1]Note that the curves of the M-GLRT and the M-AMF start from SNR=20 dB instead of SNR=15 dB, due to their very low $P_{\rm d}$ values for SNR<20 dB.

energy leading to enhanced performances compared to the receivers which make use only one of these properties.

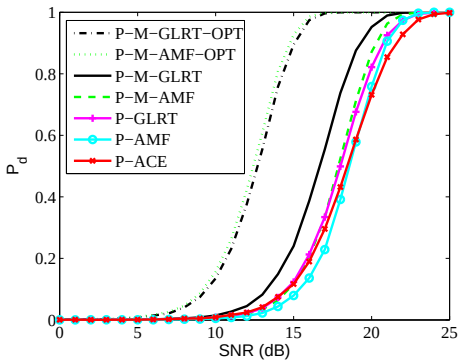

Fig. 7. $P_{\rm d}$ versus SNR for the P-M-GLRT, P-M-AMF, P-GLRT, P-AMF, and P-ACE with simulated data; $N = 17$, $K = N + 1$, $N_\epsilon = 5$, and $P_{\rm fa} = 10^{-4}$.

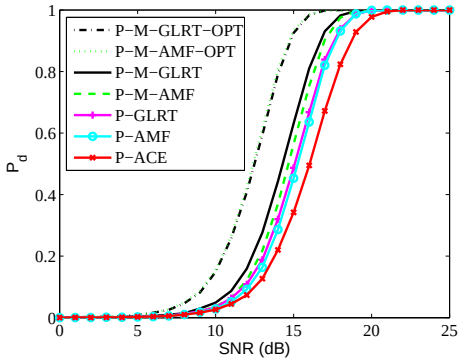

Fig. 8. RMS range error versus SNR for the P-M-GLRT, P-M-AMF, P-GLRT, P-AMF, and P-ACE with simulated data; $N = 17$, $K = 2N$, $N_\epsilon = 5$, and $P_{\rm fa} = 10^{-4}$.

B. Real dataset

In order to show the performances of detection and range estimation in a realistic environment, we exploit the experimental L-band ground clutter data collected using the MIT Lincoln Laboratory Phase One radar [49], which have been shown to exhibit a good persymmetric covariance matrix [19].

1) The Phase One radar: An overall block diagram of this radar is shown in [49] which can operate in any one of five different radar bands (VHF, UHF, L-, S-, and X-bands). The system exciter supplied all transmit and receive local oscillator (LO) frequencies and provided the basic timing reference for the system. The basic frequency reference for the exciter was a HP8662A synthesizer signal generator, with sufficient stability to support an overall clutter improvement factor of 60dB. The system had five transmitters. The signals from each of the five high-power transmitters were fed through their respective circulators to transmission lines. Several years after the Phase One measurement program was completed, the L-band component of the Phase One radar was upgraded to provide an improved LCE (L-band Clutter Experiment) instrument for the measurement of low-Doppler windblown clutter spectra to low levels of clutter spectral power [50].

TABLE I
SPECIFICATIONS OF THE ANALYZED REAL CLUTTER DATASET

	DatasetH0670372.iq
Number of Pulses N_t	30720
Number of Cells N_c	76
Polarizations	HH, VV
RF Frequency	1.23 GHz
Pulse Length	100 ns
Pulse Repetition Frequency	100 Hz
Sampling Frequency	10 MHz
Radar Scan Mode	Fixed Azimuth
Radar Azimuth Angle	235 Deg
Grazing angle	0.65 Deg
Range	2001-3125 m
Radar Beam Width	3.4 Deg
Range Resolution	15 m
Quantization Bit	13 bit
Mean/Max Wind Speed	20/20 mph

The measurements of L-band clutter were recorded in May 1985 at the Katahdin Hill site, MIT-LL. This data contained 30,720 pulses, with a pulse repetition frequency (PRF) of 500Hz. Data were recorded from 76 contiguous range gates using the L-band stationary antenna in a fixed azimuth position (235°). These 76 range cells were located from 2.0 km to 3.1 km, covering windblown trees at depression angle of 0.65°. The considered area did not contain any ground traffic targets but windblown vegetation primarily composed of mixed deciduous trees and occasional pine and cedar. Moreover, at the time of the experiment the deciduous trees did not yet had their leaves (see [49], [50] for more detailed features of this system and the experiment). Table I gives the specifications of the L-Band clutter dataset, which is used in this paper.

2) Performance on real L-band dataset: For the performance analysis, the nominal steering vector is temporal (namely $N = N_p$). We use the range cells 26-28 of VV channel as the primary data, and the range cells adjacent to the primary data as the secondary data; specifically, there are two guard cells between the primary data and secondary data. For example, we choose the range cells 15-23 and 31-39 for $K = 18$, and the range cells 7-23 and 31-47 for $K = 34$. The resulting $N(K + 3)$ data window, centered on the CUT, is slid in index N along the 30720 time pulses until the end of the dataset. The total number of different data windows is $\lfloor \frac{30720}{N} \rfloor$, where $\lfloor \cdot \rfloor$ denotes the nearest integer less than or equal to the argument. This number coincides with the total number of trials used to estimate both the number of False Alarms (FA) and the $P_{\rm d}$ of each receiver.

The performances of detection and localization are evaluated under the same number of FAs. Since the number of trials does not allow accurate estimation of the $P_{\rm fa}$, we set the threshold of the different receivers in order to obtain a pre-assigned number of FA, i.e., FA $= 18$ out of 1807 for $N = 17$, which corresponds to an obtained $P_{\rm fa}$ of about 10^{-2}. We set the Doppler frequency f at 0Hz, which is tantamount to considering the worst case of target embedded in deep clutter coinciding with the peak of the clutter power spectral density

(PSD) [51]. Note that the L-band ground clutter did not contain any returns of ground traffic targets [49]. In order to evaluate the $P_{\rm d}$, we simulate a synthetic target using the same model as Section IV-A and inject it into the 26-28th cells of VV channel. Moreover, the average SNR is defined as

$$\text{SNR}_{\text{av}} = |\alpha|^2 \boldsymbol{v}^H \widetilde{\boldsymbol{M}}^{-1} \boldsymbol{v}, \tag{47}$$

where $\widetilde{\boldsymbol{M}}$ is the estimated sample covariance matrix using all the returns of the range cells 26-28 of VV channel, and the steering vector $\boldsymbol{v}$ is defined in (41).

In summary, our simulator requires α, N, K, T_p, f, $\boldsymbol{v}$, N_ϵ, the threshold η for given FA rate as input and compute the $P_{\rm d}$ of the P-M-GLRT/P-M-AMF versus SNR_{av} as follows. We first generate $\boldsymbol{Z}_L$ and $\boldsymbol{Z}_K$ using (44) and (45). The difference with respect to Section IV-A is that the noise samples $\boldsymbol{n}_i$, $i = l-1, l, l+1$ and $\boldsymbol{n}_k$, $k = 1, \ldots, K$ are from the real L-band data of VV channel instead of simulated data. We then calculate the decision statistic of the P-M-GLRT/P-M-AMF for all $\epsilon \in \Omega$, and use the procedure in *Remark 4* and count d as the number of times that the maximum these value $\epsilon \in \Omega$ is larger than η. Finally, the $P_{\rm d}$ is calculated using by $P_{\rm d} = \sum_{k=1}^{n_e} d/n_e$, where $n_e = \left\lfloor \frac{30720}{N} \right\rfloor$ is the number of trials. Otherwise stated the procedure of computing the RMS range errors is not reported here for the sake of brevity.

Figures 9–12 show the $P_{\rm d}$ and the range RMS errors of different detectors versus SNR_{av} for $N = 17$, $N_\epsilon = 5$, and $\text{FA} = 18$ and two values of K. More precisely, Figures 9 and 10 assume $K = N + 1$, and Figures 11 and 12 refer to $K = 2N$. The curves in Figures 9–12 show that the P-M-GLRT and P-M-AMF outperform the M-GLRT and M-AMF in detection and localization. This result reaffirms what we observed in the previous subsection on simulated data. Moreover, the P-M-GLRT has slightly lower range RMS error than the P-M-AMF for low to medium SNR values.

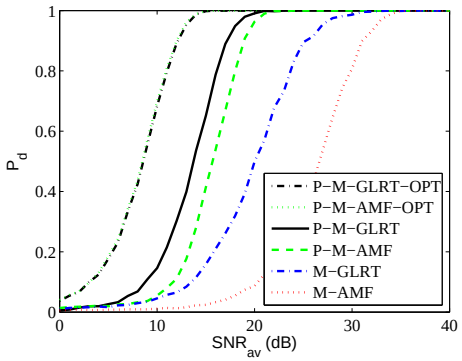

Fig. 9. $P_{\rm d}$ versus SNR_{av} for the P-M-GLRT, P-M-AMF, M-GLRT, and M-AMF with real data; $N = 17$, $K = N + 1$, $N_\epsilon = 5$, and $\text{FA} = 18$.

In Figures 13 and 14 we compare the detection performance of different persymmetric detectors with the same system parameters as in Figures 9–12. The reported curves clearly show that the proposed detectors enhance the detection performance compared with the state-of-the-art persymmetric detectors [17], [20], [23] by exploiting the spillover of target energy.

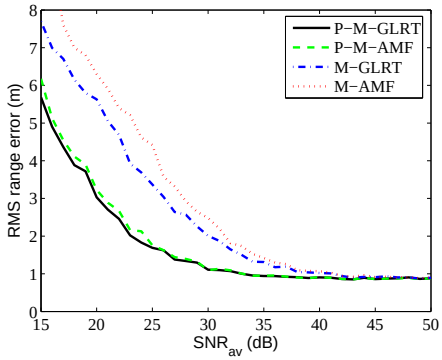

Fig. 10. RMS range error versus SNR_{av} for the P-M-GLRT, P-M-AMF, M-GLRT, and M-AMF with real data; $N = 17$, $K = N + 1$, $N_\epsilon = 5$, and $\text{FA} = 18$.

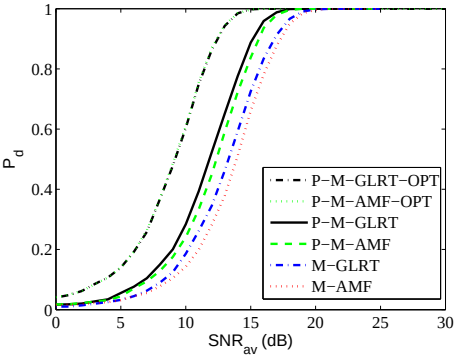

Fig. 11. $P_{\rm d}$ versus SNR_{av} for the P-M-GLRT, P-M-AMF, M-GLRT, and M-AMF with real data; $N = 17$, $K = 2N$, $N_\epsilon = 5$, and $\text{FA} = 18$.

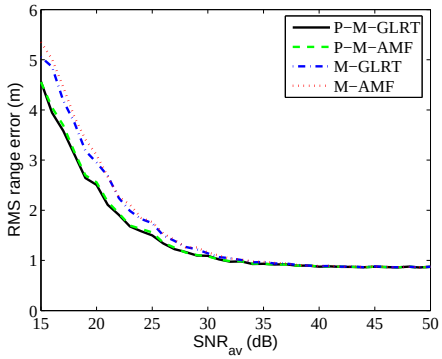

Fig. 12. RMS range error versus SNR_{av} for the P-M-GLRT, P-M-AMF, M-GLRT, and M-AMF with real data; $N = 17$, $K = 2N$, $N_\epsilon = 5$, and $\text{FA} = 18$.

In most practical case the number of the secondary data snapshots is more than the size of the covariance matrix and thereby the rank of (19) is full with probability one. However, exact performance analysis seems to be very complicated if possible at all. Even using random matrix theory, the asymptotic impact of the distribution of the eigenvalues of (19) on the detection performance is not easy to track. Moreover, our simulations and experiments for two cases ($K = N + 1$

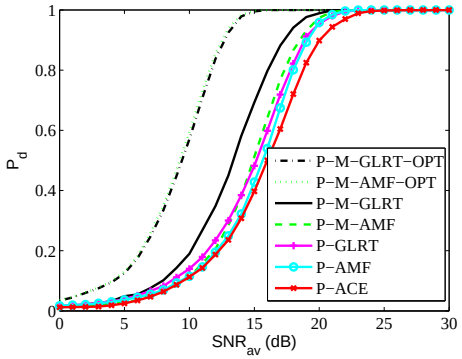

Fig. 13. $P_{\rm d}$ versus $\mathrm{SNR}_{\rm av}$ for the P-M-GLRT, P-M-AMF, P-GLRT, P-AMF, and P-ACE with real data; $N = 17$, $K = N + 1$, $N_\epsilon = 5$, and FA $= 18$.

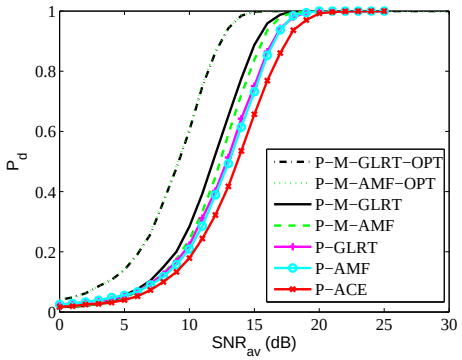

Fig. 14. $P_{\rm d}$ versus $\mathrm{SNR}_{\rm av}$ for the P-M-GLRT, P-M-AMF, P-GLRT, P-AMF, and P-ACE with real data; $N = 17$, $K = 2N$, $N_\epsilon = 5$, and FA $= 18$.

and $K = 2N$) have always resulted in a full-rank covariance estimate of the disturbance. Note that, the persymmetric detectors can work in some cases of $K < N$. Even for some cases where the sample covariance matrix is not full rank, the additional information about the persymmetric structure of the covariance matrix allows to obtain a full rank estimate of the unknown covariance matrix. To best of our knowledge, the reduced dimension/rank methods are mainly applied in the field of STAP filtering. We further investigated and found some papers that apply some reduced dimension/rank techniques in adaptive detection [45]–[48]. There are similarities between these methods and the persymmetric methods, namely, they both can reduce computational complexity and can improve the robustness in training-limited scenarios.

Since we use a grid search, the localization error includes a quantization error component which may be viewed as uniformly distributed. This is why we observe that the RMS error is larger than $\frac{T_p c}{8\sqrt{3}N_\epsilon}$. Thus, at high SNRs we propose to increase N_ϵ in order to improve the localization error at the expense of some increase in the computational cost. Moreover, we observe that the required SNR for a reasonable detection probability in Figures 3, 5, 9 and 11 increases as the number of available secondary samples reduces or as the size of the unknown covariance matrix increases. It turns out that the proposed methods require significantly less SNR compared with their counterparts.

V. Conclusions

In this paper, we have proposed new methods for adaptive detection and range estimation of a small target buried in Gaussian disturbance with unknown covariance matrix using a small training data set. In order to derive these new GLRT detectors, we jointly exploit the spillover of target energy to consecutive range samples as well as the persymmetric property of the unknown covariance matrix. Notably, these detectors possess the CFAR property with respect to the unknown parameters of the disturbance. Moreover, they demand less computational complexity than the state-of-the-art counterparts which do not exploit the persymmetric property because the operations in the proposed methods are with real values instead of complex numbers. The performance assessment, carried out using simulated data (using a complex Gaussian models), and the measured MIT dataset (a dataset with challenging heterogeneous effects found in real-world environments) shows that the proposed persymmetric detectors result in significant performance enhancements in terms of both probability of detection and localization accuracy with respect to their unstructured counterparts in open literature. Moreover, they outperform the state-of-the-art persymmetric detectors which ignore the spillover. As a final remark, possible future research tracks might include the design of joint algorithms for detection and localization for non-Gaussian scenarios [52], as well as polarization processing [53]. Besides, the possibility of employing reduced dimension/rank techniques in combination with the energy spilover and presymetry is a good idea for future further investigations. It is also of interest to compare the proposed methods to reduced dimension/rank STAP methods in [45]–[48].

Acknowledgements

We thank Dr. Danilo Orlando for his insightful suggestions to improve the quality of this paper. We also thank the Associate Editor Shannon Blunt and three anonymous referees who provided insightful comments and constructive criticisms that greatly improved the manuscript. This work was supported by the National Natural Science Foundation of China under Grant Nos. 61172166 and 61302158.

Appendix

Appendix A: Derivation of the closed-form estimate of $\boldsymbol{\alpha}_p$

The aim of this Appendix is the derivation of $\widehat{\boldsymbol{\alpha}}_p$ given by (26). To this end, observe that the derivative of (25) with respect to $\boldsymbol{\alpha}_p^T$ is given by

$$\begin{aligned}&\frac{\partial}{\partial \boldsymbol{\alpha}_p^T}\ \boldsymbol{v}^H \boldsymbol{S}_p^{-1}\boldsymbol{F}\boldsymbol{Q}^{-1}\boldsymbol{F}^H\boldsymbol{S}_p^{-1}\boldsymbol{v}\\ &= (\boldsymbol{v}^H\boldsymbol{S}_p^{-1}\boldsymbol{v})\boldsymbol{D}^T(\epsilon)\boldsymbol{Q}^{-1}\boldsymbol{F}^H\boldsymbol{S}_p^{-1}\boldsymbol{v}\\ &= (\boldsymbol{v}^H\boldsymbol{S}_p^{-1}\boldsymbol{v})\big(\boldsymbol{D}^T(\epsilon)\boldsymbol{Q}^{-1}\boldsymbol{X}_P^H\boldsymbol{S}_p^{-1}\boldsymbol{v}\\ &\quad -\boldsymbol{D}^T(\epsilon)\boldsymbol{Q}^{-1}\boldsymbol{D}^*(\epsilon)\boldsymbol{\alpha}_p^H\boldsymbol{v}^H\boldsymbol{S}_p^{-1}\boldsymbol{v}\big).\end{aligned} \tag{48}$$

Since the matrix $\boldsymbol{Q}$ is positive definite, and $\boldsymbol{D}(\epsilon)$ has full column rank, it follows that $\boldsymbol{D}^T(\epsilon)\boldsymbol{Q}^{-1}\boldsymbol{D}^*(\epsilon)$ is positive definite and invertible. Setting to zero the derivative of (48), yields

$$\widehat{\boldsymbol{\alpha}}_p^H = \frac{\left[\boldsymbol{D}^T(\epsilon)\boldsymbol{Q}^{-1}\boldsymbol{D}^*(\epsilon)\right]^{-1}\boldsymbol{D}^T(\epsilon)\boldsymbol{Q}^{-1}\boldsymbol{X}_p^H\boldsymbol{S}_p^{-1}\boldsymbol{v}}{\boldsymbol{v}^H\boldsymbol{S}_p^{-1}\boldsymbol{v}}, \quad (49)$$

which is the conjugate transpose form of (26).

Appendix B: Derivation of (30)

By using (26) and Appendix A, we have

$$f_1(\boldsymbol{Z};\widehat{\boldsymbol{M}},\widehat{\boldsymbol{\alpha}}_p,\epsilon) \propto \{\det[\boldsymbol{S}_p]\det[\boldsymbol{Q}]\}^{-(K+3)} \times \left[1+\frac{\boldsymbol{v}^H\boldsymbol{S}_p^{-1}\boldsymbol{X}_p\left(\boldsymbol{Q}^{-1}-\boldsymbol{P}\right)\boldsymbol{X}_p^H\boldsymbol{S}_p^{-1}\boldsymbol{v}}{\boldsymbol{v}^H\boldsymbol{S}_p^{-1}\boldsymbol{v}}\right]^{-(K+3)} \quad (50)$$

where

$$\boldsymbol{P} = \boldsymbol{Q}^{-1}\boldsymbol{D}^*(\epsilon)\left[\boldsymbol{D}^T(\epsilon)\boldsymbol{Q}^{-1}\boldsymbol{D}^*(\epsilon)\right]^{-1}\boldsymbol{D}^T(\epsilon)\boldsymbol{Q}^{-1}. \quad (51)$$

Moreover, $f_0(\boldsymbol{Z};\widehat{\boldsymbol{M}})$ can be recast as

$$f_0(\boldsymbol{Z};\widehat{\boldsymbol{M}}) \propto \{\det[\boldsymbol{S}_p]\det[\boldsymbol{Q}]\}^{-(K+3)} \times \left[1+\frac{\boldsymbol{v}^H\boldsymbol{S}_p^{-1}\boldsymbol{X}_p\boldsymbol{Q}^{-1}\boldsymbol{X}_p^H\boldsymbol{S}_p^{-1}\boldsymbol{v}}{\boldsymbol{v}^H\boldsymbol{S}_p^{-1}\boldsymbol{v}}\right]^{-(K+3)} \quad (52)$$

It follows that (29) can be recast as

$$\max_{\epsilon\in[-T_p/2,T_p/2]} \frac{\boldsymbol{v}^H\boldsymbol{S}_p^{-1}\boldsymbol{v}+\boldsymbol{v}^H\boldsymbol{S}_p^{-1}\boldsymbol{X}_p\boldsymbol{Q}^{-1}\boldsymbol{X}_p^H\boldsymbol{S}_p^{-1}\boldsymbol{v}}{\boldsymbol{v}^H\boldsymbol{S}_p^{-1}\boldsymbol{v}+\boldsymbol{v}^H\boldsymbol{S}_p^{-1}\boldsymbol{X}_p\left(\boldsymbol{Q}^{-1}-\boldsymbol{P}\right)\boldsymbol{X}_p^H\boldsymbol{S}_p^{-1}\boldsymbol{v}}, \quad (53)$$

which is equivalent to (30).

Appendix C: Derivations of (36) and (38)

In this appendix, we first give the proof of (36). To this end, multiplying out the left-hand side (LHS) of (36), we have

$$\begin{aligned}&\mathrm{tr}\left[\boldsymbol{M}^{-1}\left(\boldsymbol{F}\boldsymbol{F}^H\right)\right]\\ &=\mathrm{tr}\left[\boldsymbol{X}_p^H\boldsymbol{M}^{-1}\boldsymbol{X}_p\right]+(\boldsymbol{v}^H\boldsymbol{M}^{-1}\boldsymbol{v})\mathrm{tr}\left[\boldsymbol{D}^*(\epsilon)\boldsymbol{\alpha}_p^H\boldsymbol{\alpha}_p\boldsymbol{D}^T(\epsilon)\right]\\ &\quad-\mathrm{tr}\left[\boldsymbol{D}^*(\epsilon)\boldsymbol{\alpha}_p^H\boldsymbol{v}^H\boldsymbol{M}^{-1}\boldsymbol{X}_p\right]-\mathrm{tr}\left[\boldsymbol{X}_p^H\boldsymbol{M}^{-1}\boldsymbol{v}\boldsymbol{\alpha}_p\boldsymbol{D}^T(\epsilon)\right].\end{aligned} \quad (54)$$

On the other hand, using $\mathrm{tr}\,[\boldsymbol{A}\boldsymbol{B}]=\mathrm{tr}\,[\boldsymbol{B}\boldsymbol{A}]$, we obtain

$$\begin{aligned}&(\boldsymbol{v}^H\boldsymbol{M}^{-1}\boldsymbol{v})\mathrm{tr}\left[\left([\boldsymbol{\alpha}_p-\boldsymbol{b}]\boldsymbol{D}^T(\epsilon)\right)^H\left([\boldsymbol{\alpha}_p-\boldsymbol{b}]\boldsymbol{D}^T(\epsilon)\right)\right]\\ &=(\boldsymbol{v}^H\boldsymbol{M}^{-1}\boldsymbol{v})\Big(\mathrm{tr}\left[\boldsymbol{D}^*(\epsilon)\boldsymbol{\alpha}_p^H\boldsymbol{\alpha}_p\boldsymbol{D}^T(\epsilon)\right]\\ &\qquad+\mathrm{tr}\left[\boldsymbol{D}^*(\epsilon)\boldsymbol{b}^H\boldsymbol{b}\boldsymbol{D}^T(\epsilon)\right]\Big)-\mathrm{tr}\,[\boldsymbol{A}\boldsymbol{B}]-\mathrm{tr}\,[\boldsymbol{B}\boldsymbol{C}]\\ &=(\boldsymbol{v}^H\boldsymbol{M}^{-1}\boldsymbol{v})\mathrm{tr}\left[\boldsymbol{D}^*(\epsilon)\boldsymbol{\alpha}_p^H\boldsymbol{\alpha}_p\boldsymbol{D}^T(\epsilon)\right]\\ &\quad+(\boldsymbol{v}^H\boldsymbol{M}^{-1}\boldsymbol{v})\mathrm{tr}\left[\boldsymbol{D}^*(\epsilon)\boldsymbol{b}^H\boldsymbol{b}\boldsymbol{D}^T(\epsilon)\right]\\ &\quad-\mathrm{tr}\left[\boldsymbol{D}^*(\epsilon)\boldsymbol{\alpha}_p^H\boldsymbol{v}^H\boldsymbol{M}^{-1}\boldsymbol{X}_p\right]\\ &\quad-\mathrm{tr}\left[\boldsymbol{X}_p^H\boldsymbol{M}^{-1}\boldsymbol{v}\boldsymbol{\alpha}_p\boldsymbol{D}^T(\epsilon)\right],\end{aligned} \quad (55)$$

where

$$\begin{aligned}\boldsymbol{A}&=\boldsymbol{D}^*(\epsilon)\boldsymbol{\alpha}_p^H\boldsymbol{v}^H\boldsymbol{M}^{-1}\boldsymbol{X}_p,\\ \boldsymbol{B}&=\boldsymbol{D}^*(\epsilon)\left[\boldsymbol{D}^T(\epsilon)\boldsymbol{D}^*(\epsilon)\right]^{-1}\boldsymbol{D}^T(\epsilon),\\ \boldsymbol{C}&=\boldsymbol{X}_p^H\boldsymbol{M}^{-1}\boldsymbol{v}\boldsymbol{\alpha}_p\boldsymbol{D}^T(\epsilon).\end{aligned} \quad (56)$$

By combining (54) and (55) we obtain (36).

In the following, we show that the GLRT for known $\boldsymbol{M}$ is given by (38). When $\widehat{\boldsymbol{\alpha}}_p=\boldsymbol{b}$, it is seen that

$$\begin{aligned}&\min_{\boldsymbol{\alpha}_p}\mathrm{tr}\left[\boldsymbol{M}^{-1}\left(\boldsymbol{F}\boldsymbol{F}^H\right)\right]\\ &\quad=\mathrm{tr}\left[\boldsymbol{X}_p^H\boldsymbol{M}^{-1}\boldsymbol{X}_p\right]-(\boldsymbol{v}^H\boldsymbol{M}^{-1}\boldsymbol{v})\mathrm{tr}\left[\boldsymbol{D}^*(\epsilon)\boldsymbol{b}^H\boldsymbol{b}\boldsymbol{D}^T(\epsilon)\right],\end{aligned} \quad (57)$$

which substituted into (35), yields

$$\begin{aligned}&\max_{\epsilon}\ (\boldsymbol{v}^H\boldsymbol{M}^{-1}\boldsymbol{v})\mathrm{tr}\left[\boldsymbol{D}^*(\epsilon)\boldsymbol{b}^H\boldsymbol{b}\boldsymbol{D}^T(\epsilon)\right]\\ &=\max_{\epsilon}\ \frac{\mathrm{tr}\left[\boldsymbol{B}\boldsymbol{X}_p^H\boldsymbol{M}^{-1}\boldsymbol{v}\boldsymbol{v}^H\boldsymbol{M}^{-1}\boldsymbol{X}_p\boldsymbol{B}\right]}{\boldsymbol{v}^H\boldsymbol{M}^{-1}\boldsymbol{v}}\\ &=\max_{\epsilon}\ \frac{\boldsymbol{v}^H\boldsymbol{M}^{-1}\boldsymbol{X}_p\boldsymbol{B}\boldsymbol{B}\boldsymbol{X}_p^H\boldsymbol{M}^{-1}\boldsymbol{v}}{\boldsymbol{v}^H\boldsymbol{M}^{-1}\boldsymbol{v}}.\end{aligned} \quad (58)$$

It is easy to show that (58) leads to (38).

References

[1] Reed, I. S., Mallett, J. D., and Brennan, L. E.
Rapid convergence rate in adaptive arrays.
IEEE Transactions on Aerospace and Electronic Systems, 10, 6, (Nov. 1974), 853-863.

[2] Kelly, E. J.
An adaptive detection algorithm.
IEEE Transactions on Aerospace and Electronic Systems, 22, 2 (Mar. 1986), 115-127.

[3] Robey, F. C., Fuhrman, D. L., Kelly, E. J., and Nitzberg R.
A CFAR adaptive matched filter detector.
IEEE Transactions on Aerospace and Electronic Systems, 29, 1 (Jan. 1992), 208-216.

[4] Blunt, S. D., and Gerlach, K.
Efficient Robust AMF using the FRACTA Algorithm.
IEEE Transactions on Aerospace and Electronic Systems, 41, 2 (Apr. 2005), 537-548.

[5] De Maio, A.
A new derivation of the adaptive matched filter.
IEEE Signal Processing Letters, 11, 10 (Oct. 2004), 792-793.

[6] Orlando, D., and Ricci, G.
A Rao test with enhanced selectivity properties in homogeneous scenarios.
IEEE Transactions on Signal Processing, 58, 10 (Oct. 2010), 5385-5390.

[7] De Maio, A.
Rao test for adaptive detection in gaussian interference with unknown covariance matrix.
IEEE Transactions on Signal Processing, 55, 7 (Jul. 2007), 3577-3584.

[8] Pulsone, N. B., and Rader, C. M.
Adaptive beamformer orthogonal rejection test.
IEEE Transactions on Signal Processing, 49, 3 (Mar. 2001), 521?29.

[9] Haykin, S.
Adaptive Filter Theory, (4th ed).
Englewood Cliffs, NJ: Prentice-Hall, 2002.

[10] Chong, C.
Signal Processing for MIMO Radars: Detection under Gaussian and non-Gaussian environments and application to STAP.
PhD thesis, Supelec, Nov. 2011.

[11] Rangaswamy, M., Freeman, C. L., Gerlach, K.
Robust adaptive signal processing methods for heterogeneous radar clutter scenarios.
Signal Processing, 84, 9 (Sep. 2004), 1653-1665.

[12] Greco, M., Gini, F., Rangaswamy, M.
Statistical analysis of measured polarimetric clutter data at different range resolutions.
IEE Proceedings on Radar, Sonar and Navigation, 153, 6 (Dec. 2006), 473-481.

[13] Liu, W., Xie, W., and Wang, Y.
Parametric detector in the situation of mismatched signals.
IET Radar, Sonar and Navigation, 8, 1 (Jan. 2014), 48-53.

[14] De Maio, A.
Maximum likelihood estimation of structured persymmetric covariance matrices.
Signal Processing, 83, 3 (Mar. 2003), 633-640.

[15] Hao, C., Orlando, D., Ma, X., and Hou, C.
Persymmetric Rao and Wald tests for partially homogeneous environment.
IEEE Signal Processing Letters, 19, 9 (Sep. 2012), 587-590.

[16] Nitzberg, R.
Application of maximum likelihood estimation of persymmetric covariance matrices to adaptive processing.
IEEE Transactions on Aerospace and Electronic Systems, 16, 1 (Jan. 1980), 124-127.

[17] Cai, L., and Wang, H.
A persymmetric multiband GLR algorithm.
IEEE Transactions on Aerospace and Electronic Systems, 28 3, (Jul. 1992), 806-816.

[18] Casillo, M., De Maio, A., Iommelli, S., and Landi, L.
A persymmetric GLRT for adaptive detection in partially-homogeneous environment.
IEEE Signal Processing Letter, 14, 12 (Dec. 2007), 1016-1019.

[19] Hao, C., Orlando, D., Ma, X., Yan, S., and Hou, C.
Persymmetric adaptive detection of distributed targets in partially-homogeneous environment.
Digital signal processing, 24, 1 (Jan. 2014), 42-51.

[20] Gao, Y., Liao, G., Zhu, S., Zhang, X., and Yang, D.
Persymmetric adaptive detectors in homogeneous and partially homogeneous environments.
IEEE Transactions on Signal Processing, 62, 2 (Feb. 2014), 331-342.

[21] Conte, E., and De Maio, A.
Exploiting persymmetry for CFAR detection in compound-Gaussian clutter.
IEEE Transactions on Aerospace and Electronic Systems, 39, 2 (Apr. 2003), 719-724.

[22] Gao, Y., Liao, G., Zhu, S., and Yang, D.
A persymmetric GLRT for adaptive detection in compound-Gaussian clutter with random texture.
IEEE Signal Processing Letters, 20, 6 (Jun. 2013), 615-618.

[23] Pailloux, G., Forster, P., Ovarlez, J., and Pascal, F.
Persymmetric adaptive radar detectors.
IEEE Transactions on Aerospace and Electronic Systems, 47, 4 (Oct. 2011), 2376-2390.

[24] Wang, P., Sahinoglu, Z., Pun, M., and Li, H.
Persymmetric parametric adaptive matched filter for multichannel adaptive signal detection.
IEEE Transactions on Signal Processing, 60, 6 (Jul. 2012), 3322-3328.

[25] Hao, C., Orlando, D., Foglia, G., Ma, X., Yan, S., and Hou, C.
Persymmetric detectors with enhanced rejection capabilities.
IET Radar, Sonar and Navigation, 8, 5 (Jun. 2014), 557-563.

[26] De Maio, A., and Orlado, D.
An Invariant Approach to Adaptive Radar Detection Under Covariance Persymmetry.
IEEE Transactions on Signal Processing, 63, 5 (Jan. 2015), 1297-1309.

[27] Richards, M. A., Scheer, J. A., and Holm, W. A.
Principles of Modern Radar: Basic Principles.
Scitech Publishing, Inc., 2010.

[28] Cann, A. J.
Range gate straddling loss and joint probability with partial correlation.
IEEE Transactions on Aerospace and Electronic Systems, 38, 3 (July 2002), 1054-1058.

[29] Zhang, X., Willett, P. K., and Bar-Shalom, Y.
Detection and localization of multiple unresolved extended targets via monopulse radar signal processing.
IEEE Transactions on Aerospace and Electronics Systems, 45, 2 (Apr. 2009), 455-472.

[30] Orlando, D., and Ricci, G.
Adaptive radar detection and localization of a point-like target.
IEEE Transactions on Signal Processing, 59, 9 (Sep. 2011), 4086-4096.

[31] Ward, J.
Space-time adaptive processing for airborne radar.
MIT, Lexington, MA, Technical Report 1015, Dec. 13, 1994.

[32] Gerlach, K. R., Blunt, S. D., and Picciolo, M. L.
Robust Adaptive Matched Filtering using the FRACTA Algorithm.
IEEE Transactions on Aerospace and Electronic Systems, 40, 3 (Jul. 2004), 929-945.

[33] Coco, M. D., Orlando, D., and Ricci, G.
A tracking system exploiting interaction between a detector with localization capabilities and KF.
IEEE Transactions on Signal Processing, 60, 11 (Nov. 2012), 6031-6036.

[34] Daun, M., Nickel, U., and Koch, W.
Tracking in multistatic passive radar systems using DAB/DVB-T illumination.
Signal Processing, 92, 6 (Jun. 2012), 1365-1386.

[35] Orlando, D., Ricci, G., and Bar-Shalom, Y.
Track-before-detect algorithms for targets with kinematic constraints.
IEEE Transactions on Aerospace and Electronics Systems, 47, 3 (Jul. 2011), 1837-1849.

[36] Orlando, D., Venturino, L., Lops, M., and Ricci G.
Track-before-detect strategies for STAP radars.
IEEE Transactions on Signal Processing, 58, 2 (Feb. 2010), 933ł938.

[37] Bandiera, F., Mancino, M., and Ricci, G.
Localization strategies for multiple point-like radar targets.
IEEE Transactions on Signal Processing, 60, 12 (Dec. 2012), 6708-6712.

[38] Aubry, A., De Maio, A., Pallotta, L., and Farina, A.
Radar detection of distributed targets in homogeneous interference whose inverse covariance structure is defined via unitary invariant functions.
IEEE Transactions on Signal Processing, 61, 10 (Oct. 2013), 4949-4961.

[39] Bandiera, F., Orlando, D., and Ricci, G.
Advanced radar detection schemes under mismatched signal models.
Synthesis Lectures on Signal Processing No. 8, Morgan & Claypool Publishers, 2009.

[40] Farina, A.
Antenna-based signal processing techniques for radar systems.
Boston, MA: Artech House, 1992.

[41] Levanon, N.
Radar principles.
John Wiley & Sons, 1988.

[42] Van Trees, H. L.
Detection, estimation, and modulation theory, part I.
New York: Wiley, 2001.

[43] Anderson, T.W.
An introduction to multivariate statistical analysis (3rd ed).
New York: Wiley, 2003.

[44] Golub, G. H., and Van Loan, C. F.
Matrix Computations, 2nd ed.
Baltimore, MD: Johns Hopkins Univ. Press, 1989.

[45] Reed, I. S., and Gau, Y. L.
A fast CFAR detection space-time adaptive processing algorithm.
IEEE Transactions on Signal Processing, 47, 1999, 1151-1154.

[46] Gau, Y. L., and Reed, I. S.
An improved reduced-rank CFAR space-time adaptive radar detection algorithm.
IEEE Transactions on Signal Processing, 46, 1998, 2139-2146.

[47] Fa, R., de Lamare, R., and Wang, L.
Reduced-Rank STAP Schemes for Airborne Radar Based on Switched Joint Interpolation, Decimation and Filtering Algorithm.
IEEE Transactions on Signal Processing, 58, 8 (Aug. 2010), 4182-4194.

[48] Wang, Y., Liu, W., Xie, W., and Zhao, Y.
Reduced-rank space-time adaptive detection for airborne radar.
Science China, Information Sciences, 57, 8 (Aug. 2014), 082310(11).

[49] Billingsley, J.B., Farina, A., Gini, F., Greco, M., and Verrazzani, L.
Statistical analyses of measured radar ground clutter data.
IEEE Transactions on Aerospace and Electronic Systems, 35, 2 (Apr. 1999), 579-593.

[50] Billingsley, J. B.
Low-Angle Radar Land Clutter.
Raleigh, NC: Scitech Publishing, 2002.

[51] De Maio, A., Foglia, G., Conte, E., and Farina, A.
CFAR behavior of adaptive detectors: an experimental analysis.
IEEE Transactions on Aerospace and Electronics Systems, 41, 1 (Jan. 2005), 233-251.

[52] Watts, S.
Radar detection prediction in K-distributed sea clutter and thermal noise.

IEEE Transactions on Aerospace and Electronic Systems, 23, 1 (Jan. 1987), 40-45.

[53] Lombardo, P., Pastina, D., and Bucciarelli, T.
Adaptive polarimetric target detection with coherent radar. II. Detection against non-Gaussian background.
IEEE Transactions on Aerospace and Electronic Systems, 37, 4 (Oct. 2001), 1207-1220.

Chengpeng Hao

Chengpeng Hao (M'08) received the B.S. and the M.S. degrees in electronic engineering from Beijing Broadcasting Institute, Beijing, China, in 1998 and 2001 respectively. He received the Ph.D. degree in signal and information processing from Institute of Acoustics, Chinese Academy of Sciences, Beijing, China, in 2004. He is currently a professor of the State Key Laboratory of Information Technology for Autonomous Underwater vehicles, Chinese Academy of Sciences. His research interests are in the field of statistical signal processing with more emphasis on adaptive sonar and radar signal processing. He has held a visiting position with the Electrical and Computer Engineering Department, Queens University, Kingston, Canada (July 2013-July 2014).

Saeed Gazor

Saeed Gazor (S'94-M'95-SM'98) received the B.Sc. degree in electronics engineering in 1987 and the M.Sc. degree in communication systems engineering in 1989, from Isfahan University of Technology, both summa cum laude,, the highest honors. He received the Ph.D. degree in signal and image processing from Telecom Paris, Dpartement Signal (cole Nationale Suprieure des Tlcommunications/ENST, Paris), France, in 1994. Since 1999, he has been on the Faculty at Queens University at Kingston, Ontario, Canada, and currently holds the position of full Professor of the Department of Electrical and Computer Engineering and is also cross-appointed to the Department of Mathematics and Statistics at Queens University. His main research interests are statistical and adaptive signal processing, detection and estimation theory, cognitive signal processing, array signal processing, speech processing, and information theory etc. Dr. Gazor's research has earned him a number of awards including; a Provincial Premier's Research Excellence Award, a Canadian Foundation of Innovation Award, an Ontario Innovation Trust Award, and an Intel Research Excellence Award. He is a member of Professional Engineers Ontario. He has been on the Technical Program Committee of numerous conferences and has served as an Organizing Committee member of many international conferences in various capacities, such as Publication Chair for the 11th IEEE ISSPA 2012 in Montreal and 26th BSC 2012 in Kingston, Technical Program (Co-)Chair for the IEEE WoSPA 2011 in Algeria, 24th BSC 2008 in Ontario, and the 11th IEEE ISSPA 2012. He was also the Special Sessions Chair for ISSPA 2012. He served as a Guest Editor for the IEEE JOURNAL ON SELECTED AREAS IN COMMUNICATIONS for the issue on Theories and Methods for Advanced Wireless Relays. He is currently serving as Associate Editor for the IEEE SIGNAL PROCESSING LETTERS.

Goffredo Foglia

Goffredo Foglia was born in San Paolo Belsito, Italy, on November 20, 1977. He received the Dr. Eng. degree in June 2003 from the University of Naples Federico II, and the Ph.D. degree in information engineering in February 2007 from the University of Cassino, Italy. In February 2004 he joined Elettronica S.p.A., Rome, Italy. Today he is responsible for the Integrated Electronic Warfare System, with special emphasis on the electronic support measure functionalities, in the Research and Advanced Systems Design Department. His current research lies in the field of radar applications, EW system architectures and algorithms. He is an author of more than 20 papers in international journals and conferences.

Bin Liu

Bin Liu (M'09) received his B.E. degree (2004) and Ph.D. degree (2009) in Signal and information processing from Beijing Univ. of Posts and Telecomm. and Chinese Academy of Sciences, respectively. He was with Department of Statistical Science, Duke University as a research scholar during 2009-2010. Meanwhile, he participated in a full-year program on Sequential Monte Carlo Methodology, held

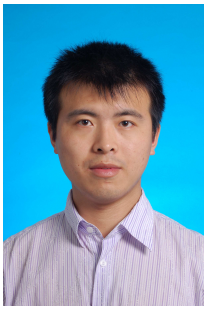

in Statistical and Applied Mathematical Sciences Institute (SAMSI). He once held an appointment of senior research fellow in Shenzhen Kuang-Chi Institute of Advanced Technology, and of senior engineer in HiSilicon Tech. Co., Ltd.. He is currently an associate professor at School of computer science and technology, Nanjing Univ. of Posts and Telecomm., Nanjing, China. His research interests include Bayesian statistical modeling and computation algorithms with applications in interdisciplinary problems.

Chaohuan Hou

Chaohuan Hou (SM'96-F'01) received a B.Sc. degree in physics from Peking University, Beijing, China, in 1958. Since 1958, he has worked on underwater acoustics and signal processing with the IACAS, Beijing, where he became a professor in 1985. He was the Deputy Director of IACAS from 1993 to 1997. He has published more than 200 journal and conference papers. His current research interests are in underwater acoustics, digital signal processing, arrays signal processing, very-large-scale integration signal processing, and application-specific integrated circuit chip design. Prof. Hou was elected as an academician of the Chinese Academy of Sciences in 1995. He was the president of the Acoustical Society of China from 2002 to 2006 and then became the honorary president. From 2007 to 2010, he was a board member of the International Commission for Acoustics.

The caption of the figures

1) Figure 1: a) The illustration of a target straddling between two consecutive range cells n and $n+1$; b) the cross-correlation function for a rectangular pulse versus the range locations and stampeded cells.
2) Figure 2: Sampling process of the signal component assuming a unit-energy rectangular pulse waveform of duration T_p seconds.
3) Figure 3: $P_{\rm d}$ versus SNR for the P-M-GLRT, P-M-AMF, M-GLRT, and M-AMF with simulated data; $N = 17$, $K = N + 1$, $N_\epsilon = 5$, and $P_{\rm fa} = 10^{-4}$.
4) Figure 4: RMS range error versus SNR for the P-M-GLRT, P-M-AMF, M-GLRT, and M-AMF with simulated data; $N = 17$, $K = N+1$, $N_\epsilon = 5$, and $P_{\rm fa} = 10^{-4}$.
5) Figure 5: $P_{\rm d}$ versus SNR for the P-M-GLRT, P-M-AMF, M-GLRT, and M-AMF with simulated data; $N = 17$, $K = 2N$, $N_\epsilon = 5$, and $P_{\rm fa} = 10^{-4}$.
6) Figure 6: RMS range error versus SNR for the P-M-GLRT, P-M-AMF, M-GLRT, and M-AMF with simulated data; $N = 17$, $K = 2N$, $N_\epsilon = 5$, and $P_{\rm fa} = 10^{-4}$.
7) Figure 7: $P_{\rm d}$ versus SNR for the P-M-GLRT, P-M-AMF, P-GLRT, P-AMF, and P-ACE with simulated data; $N = 17$, $K = N + 1$, $N_\epsilon = 5$, and $P_{\rm fa} = 10^{-4}$.
8) Figure 8: RMS range error versus SNR for the P-M-GLRT, P-M-AMF, P-GLRT, P-AMF, and P-ACE with simulated data; $N = 17$, $K = 2N$, $N_\epsilon = 5$, and $P_{\rm fa} = 10^{-4}$.
9) Figure 9: $P_{\rm d}$ versus $\rm SNR_{av}$ for the P-M-GLRT, P-M-AMF, M-GLRT, and M-AMF with real data; $N = 17$, $K = N + 1$, $N_\epsilon = 5$, and FA $= 18$.
10) Figure 10: RMS range error versus $\rm SNR_{av}$ for the P-M-GLRT, P-M-AMF, M-GLRT, and M-AMF with real data; $N = 17$, $K = N + 1$, $N_\epsilon = 5$, and FA $= 18$.
11) Figure 11: $P_{\rm d}$ versus $\rm SNR_{av}$ for the P-M-GLRT, P-M-AMF, M-GLRT, and M-AMF with real data; $N = 17$, $K = 2N$, $N_\epsilon = 5$, and FA $= 18$.
12) Figure 12: RMS range error versus $\rm SNR_{av}$ for the P-M-GLRT, P-M-AMF, M-GLRT, and M-AMF with real data; $N = 17$, $K = 2N$, $N_\epsilon = 5$, and FA $= 18$.
13) Figure 13: $P_{\rm d}$ versus $\rm SNR_{av}$ for the P-M-GLRT, P-M-AMF, P-GLRT, P-AMF, and P-ACE with real data; $N = 17$, $K = N + 1$, $N_\epsilon = 5$, and FA $= 18$.
14) Figure 14: $P_{\rm d}$ versus $\rm SNR_{av}$ for the P-M-GLRT, P-M-AMF, P-GLRT, P-AMF, and P-ACE with real data; $N = 17$, $K = 2N$, $N_\epsilon = 5$, and FA $= 18$.